A superconducting quantum interference device magnetometer system for quantitative analysis and imaging of hidden corrosion activity in aircraft aluminum structures

A. Abedi and J. J. Fellenstein
Department of Physics and Astronomy, Vanderbilt University, Nashville, Tennessee 37235

A. J. Lucas
NCI Information Systems, Inc., Suite 505, 131 Russell Parkway, Warner Robins, Georgia 31088

J. P. Wikswo, Jr.
Department of Physics and Astronomy, Vanderbilt University, Nashville, Tennessee 37235

(Received 31 March 1999; accepted for publication 12 September 1999)

We have designed and built a magnetic imaging system for quantitative analysis of the rate of ongoing hidden corrosion of aircraft aluminum alloys in planar structures such as intact aircraft lap joints. The system utilizes a superconducting quantum interference device (SQUID) magnetometer that measures the magnetic field associated with corrosion currents. It consists of a three-axis (vector) SQUID differential magnetometer, magnetic, and rf shielding, a computer controlled x-y stage, sample registration, and positioning mechanisms, and data acquisition and analysis software. The system is capable of scanning planar samples with dimensions of up to 28 cm square, with a spatial resolution of 2 mm, and a sensitivity of 0.3 pT/Hz$^{1/2}$ (at 10 Hz). In this article we report the design and technical issues related to this system, outline important data acquisition techniques and criteria for accurate measurements of the rate of corrosion, especially for weakly corroding samples, and present preliminary measurements.
[S0034-6748(99)04312-9]

I. INTRODUCTION

The detection of ongoing hidden corrosion and measurement of its rate are extremely important to military and commercial aircraft for both safety and economic reasons. With the increase in the number of aging aircraft, for example, the risk of structural weakening and failure due to undetected corrosion-related damage is increasing. Addressing potential safety concerns requires not only the measurement of existing corrosion damage, typically through nondestructive testing (NDT), but also measurement of the rates of ongoing corrosion and how these rates are affected by environmental factors. Although standard electrochemical instruments and techniques are well suited for studying corrosion on the exposed surface of samples, they are of little use for crevice or hidden corrosion, where the corrosion activity is governed by the restricted nature of the inaccessible chemical environment surrounding the corroding surfaces. Since an invasive examination would alter the chemical environment and affect the rate and distribution of corrosion in such situations, superconducting quantum interference device (SQUID) magnetometers provide a powerful technique for nondestructive, quantitative analysis of corrosion rates and for studying the spatiotemporal variations of corrosion activity. Furthermore, SQUID magnetometers can detect hidden corrosion from its onset, long before there has been sufficient material loss or deposition of corrosion products to allow its detection by other noninvasive techniques. The unrivaled sensitivity of SQUID magnetometers promises the possibility for quantitative analysis of corrosion at realistic rates and in typical environments without the need for time-consuming field-test coupons or unrealistic accelerated tests. The ability of SQUIDs to rapidly scan large areas with high sensitivity makes them ideal for many magnetic imaging applications.[1]

Previous qualitative studies have shown that SQUID magnetometers have the sensitivity to detect noninvasively the magnetic field associated with corrosion currents in various metal-acid and metal-salt environments.[2–4] These studies were done using strong corrosive solutions to produce high rates of corrosion and focused primarily on geometries which were intended to maximize the magnetic field generated by corrosion and to simplify its interpretation. Nevertheless, they presented the possibility of the use of SQUIDs for noninvasive studies of hidden corrosion. Other studies have demonstrated the possibility of the use of SQUIDs for cyclic voltametry,[5] and for evaluation of electrochemical reactivity of materials, such as 304 stainless steel.[6] The first SQUID magnetometer specifically designed for corrosion studies was constructed by Quantum Magnetics (San Diego, CA) with a spatial resolution of the order of 1 mm and sensitivity of 3 pT/Hz$^{1/2}$ (at 1 Hz).[7] The system was operated in a nonshielded laboratory environment and was equipped with a nonmagnetic stage and computer control. A unique feature of this system was that the detection coil array was oriented at 45° with respect to the dewar axis, and the dewar was mounted at a 45° angle upon a cradle. A 180° rotation of the dewar about its axis would change the coil axis from vertical to horizontal, allowing for measurement of either of two orthogonal field components. With the coil axis in the

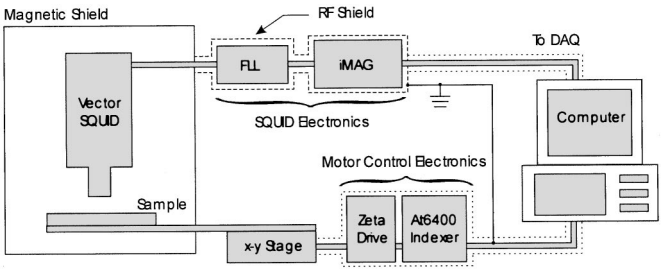

FIG. 1. The magnetic imaging system consists of a three-axis (vector) SQUID differential magnetometer, magnetic and rf shielding, a computer controlled x-y stage, sample registration and positioning system, and data acquisition and analysis capability.

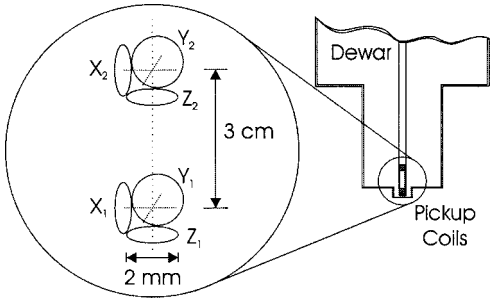

FIG. 2. The first-order differential vector magnetometer used in this system utilizes 2-mm-diameter pickup coils and a 3 cm baseline. The z (vertical) coils form an axial gradiometer, while the x and y (horizontal) coils form a planar gradiometer. The minimum coil-to-room temperature distance is 2 mm.

horizontal position, the sample could be oriented so that its corroding surface was vertical, thereby preventing problems from bubble accumulation associated with high corrosion rates.

Since the background field and environmental noise were reported to be the limiting factors for SQUID corrosion studies,[3] the first qualitative studies at Vanderbilt were conducted using a high-resolution magnetometer and magnetic shield system,[8,9] which was originally designed for measuring the magnetic fields from isolated biological tissue, such as the heart, and for the nondestructive evaluation (NDE) of materials. These studies focused on detection and imaging of magnetic fields due to corrosion of aircraft aluminum alloys.[10–13]

The system we describe in this article was designed specifically for high-resolution, long-term, noninvasive, and quantitative spatiotemporal analysis of the rate of hidden corrosion in aircraft aluminum alloys in planar structures such as aircraft lap joints. Since our primary goal was to study actual or simulated lap joints, we designed the system for these realistic sample geometries, rather than those optimized to produce a large magnetic field. Within this constraint, we would also be able to examine any other planar corrosion geometries. As with our earlier system, we chose to include a magnetic shield so that we could detect corrosion in realistic and, in particular, weakly corrosive environments. Long-term magnetic studies of ongoing corrosion require accurate and repeatable sample positioning; hence, the sample registration and positioning mechanism was designed with this in mind. This mechanism also allows for parallel, long-term study and imaging of multiple samples. In this article, we report the design and technical issues related to this system and submit a representative sample of preliminary data.

II. MAGNETIC IMAGING SYSTEM

As shown in Fig. 1, the magnetic imaging system consists of a vector SQUID magnetometer, magnetic and rf shielding, a computer controlled x-y stage, sample registration and positioning mechanisms, and data acquisition and analysis software. All the scanning and data acquisition parameters are controlled through the computer software that we developed. Planar samples (up to $28\times28\times2$ cm) are scanned under the magnetometer by the sample scanning and registration system. The system is automated to scan the sample at user-defined intervals and produces a series of two-dimensional raster images of components of magnetic field above the corroding sample. Each scan provides an image of the spatial distribution of the magnetic field within the time required to complete a raster scan. Appropriate analysis techniques are then used to quantify the rate of hidden corrosion, and to examine the spatiotemporal characteristics of its associated currents. The following sections discuss the details of the system design and components.

A. SQUID magnetometer

The custom-built vector SQUID magnetometer (Conductus Instrumentation and Systems Division, San Diego, CA, now Tristan Technologies, Inc.) was designed to provide high field sensitivity (300 fT/Hz$^{1/2}$ at 10 Hz), with spatial resolution of approximately 2 mm for corrosion studies. It is a three-axis, first-order differential magnetometer system; each axis uses a pair of 2-mm-diameter pickup coils separated vertically by a 3 cm baseline. As shown in Fig. 2, the z-component (vertical axis) pickup coils form an axial gradiometer configuration, whereas the x- and y-component (horizontal axes) pickup coils form planar gradiometers.[14] The SQUID is controlled by a flux-locked loop (FLL), mounted adjacent to the magnetic shield, and the SQUID controller (iMAG), which provides for the tuning of the SQUID, SQUID reset, trapped flux removal (by heating the SQUIDs), dc offset, low and high pass filtering, and amplification. Furthermore, these functions can be controlled by external GPIB commands. The minimum operational distance between the z pickup coil and room temperature is 2 mm.

Although a Dewar design[7] (described above) seemed attractive, it has the disadvantage that the increased complexity of the dewar and the need for a larger magnetic shield dramatically increases the cost of the system. Therefore, since our system was designed mostly to deal with small corrosion rates, where the bubble problem is not significant, our conventional design for the Dewar allowed for more efficient use of the shielded volume and reduced the cost of the system by a significant factor.

B. Sample scanning and registration system

The sample scanning system, illustrated in Fig. 3, was designed to provide repeatable scans with positioning accu-

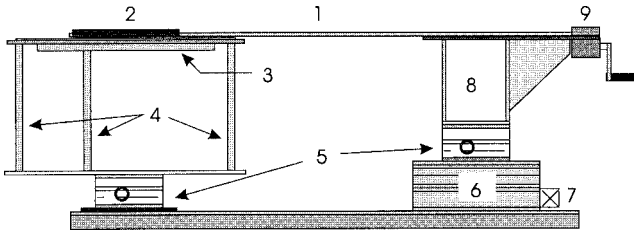

FIG. 3. The sample scanning and registration system consists of a computer-controlled x-y stage, which scans the sample over the scanning table via a rigid track. The system was designed to allow for repeated removal and repositioning of multiple samples with positioning and scanning accuracy of better than 0.1 mm: (1) track, (2) sample holder, (3) scanning table, (4) support rods, (5) z stage, (6) x-y stage, (7) stepper motor, (8) stage tower, (9) pulley system.

racy of better than 0.1 mm, and to minimize the noise due to the stage motors and electronics. Furthermore, for parallel, long-term study of multiple samples, the kinematic design of the system allows for removal and repositioning of samples to their original location under the magnetometer with ease and accuracy. The details of the scanning system are discussed below.

1. Computer-controlled stage

The main component of the scanning system is an open-frame x-y stage (Model 318122AT, Daedal Division, Parker Hannifin Corp., Harrison City, PA), with 46 cm of travel in each horizontal direction, driven by two stepper motors (S57102MO, Daedal). Each stepper motor is connected to a microstepping drive amplifier (Zeta Drive, Daedal) controlled by a computer controlled indexer (AT6400, Daedal). Each axis of the stage is equipped with magnetic proximity switches that set the end-of-travel limits of the stage, and define the home position; because of the shield and the distance between the SQUID and the stage, the magnetic field of these switches is below system noise. The home position, which is the reference point from which all distances are measured, is always approached from the positive end-of-travel limits with a preset velocity and acceleration, to ensure the reproducibility of scans to better than 0.1 mm.

2. Sample scanning track

Since the stage has ferromagnetic components and the stepper motors generate magnetic noise, they were placed outside of the magnetic shield, approximately 1.5 m from the magnetometer, and their control electronics were shielded in a separate Faraday cage. As shown in Fig. 3, a 157 cm$\times$11 cm nonmagnetic and nonconductive track (to avoid inductive coupling of powerline fields into the shield), was fabricated of 1.3-cm-thick G-10 fiberglass epoxy. The track is attached at one end to the stage tower assembly, while the other end is free to slide upon the glass surface of the scanning table (described later) beneath the magnetometer. The rigid track translates the force of the stage to the sample holder and scans the sample under the magnetometer. A self-positioning latching mechanism alongside the track was designed to lock the sample holder at a specified location near the end of the track during scans. This location was selected to center the sample holder with respect to the magnetometer when the stage is at the home position. The track serves as the platform upon which the sample holder slides in and out of the shield via a pulley, drum, and kevlar cord mechanism. A precision laboratory jack (Model 281, Newport Corp., Irvine, CA) on top of the stage provides vertical height adjustment and leveling of the track with respect to the scanning table.

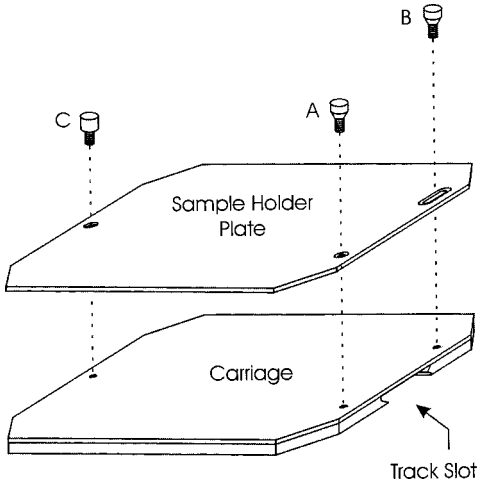

FIG. 4. The kinematic design of the sample-holder plate allows for accurate repositioning of the samples with respect to the scanning system. A carriage runs along the scanning track and has three matching threaded holes used for mounting the sample-holder plate. The beveled screw A is tightened first, then the beveled screw B, and finally the nonbeveled screw C.

3. Sample holder and kinematic design

The design of the sample holders varies in complexity depending on sample size, shape, and the desired environment (i.e., temperature, humidity) for each corroding sample, but all sample holders have a standard kinematic mounting plate by which they attached to the track. As seen in Fig. 4, the plate has a beveled hole, a beveled slot, and an oversized hole that match threaded holes in the carriage that slides along the track; two beveled screws, A and B, and one without a bevel, C, hold the plate to the carriage in a kinematic manner.

As long as the sample(s) are fixed rigidly to the sample holder, the sample holder can be removed from the carriage, and at a later time, easily repositioned to its original location. This feature allows for parallel and long-term scanning of multiple samples, each mounted on their own sample holder.

4. Scanning table

The scanning table, which provides a smooth, low-friction surface upon which track and sample holder slide, is a 85-cm-diameter nonmagnetic disk made of 1.3-cm-thick G-10, reinforced underneath for rigidity, and with a 6-mm-thick piece of plate glass on top. The table is held inside the magnetic shield by three 2.5-cm-diameter aluminum rods, which pass through the bottom of the shield and transfer the weight of the table to its support structure under the shield. Special care has been made to avoid physical contact between the magnetic shield and the scanning system to prevent stage-induced vibrations of the shield. Another precision laboratory jack (Model 281, Newport) allows for

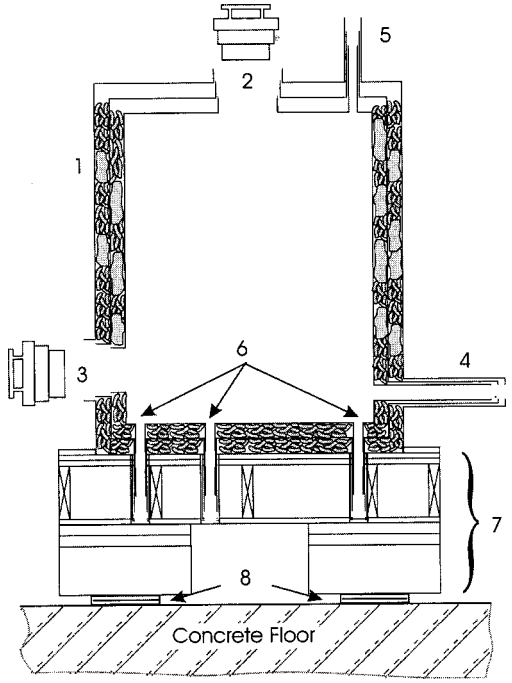

FIG. 5. The schematic diagram of the custom-built magnetic shield. The shield consists of three concentric Amumetal® cylinders. The space between the cylinders is filled with packaging pellets and sandbags to reduce shield vibrations; (1) magnetic shield; (2) liquid-cryogen-fill port with cap; (3) observation port with cap; (4) sample in/out port; (5) electronic cable port; (6) scanning-table-leg ports; (7) shield support frame; (8) vibration isolation pads.

movement of the scanning table in the *z* direction and is used for fine adjustments of the Dewar-to-sample distance. Three adjustable legs steady the support structure after the height has been set.

C. Magnetic shield

As shown in Fig. 5, the custom-built magnetic shield consists of three concentric cylinders made of high permeability Amumetal® (Amuneal Manufacturing Corp., Philadelphia, PA). The outer cylinder has a diameter of 106 cm and a height of 127 cm. Each cylinder is separated from the next by a 5-cm-gap defined by aluminum bar or ring spacers, which is filled with styrofoam packaging pellets and sandbags to reduce the amplitude of the natural modes of vibration of the shield. The shield has access ports for sample insertion/removal, observation, liquid cryogen filling, scanning table legs, and cabling; the observation and cryogen filling ports have removable, three-layer shielded covers. Three large lids on top of the shield provide full access to its interior. The shield assembly weighs approximately 500 kg, and is supported by a custom-built wooden structure, which allows the use of forklift or floor jacks to move the shield.

The shielding factors reported by the manufacturer were 51 dB for dc, and 70 dB for ac (measured at 30 Hz). The shield was de-Gaussed in our laboratory by 27 turns of 12 gauge wire that entered the shield from the observation port and exited from the sample insertion/removal port and carried a peak current of 63 A at 60 Hz. The magnitude of magnetic field measured inside the shield with fluxgate magnetometer, after de-Gaussing, was below the detection limit

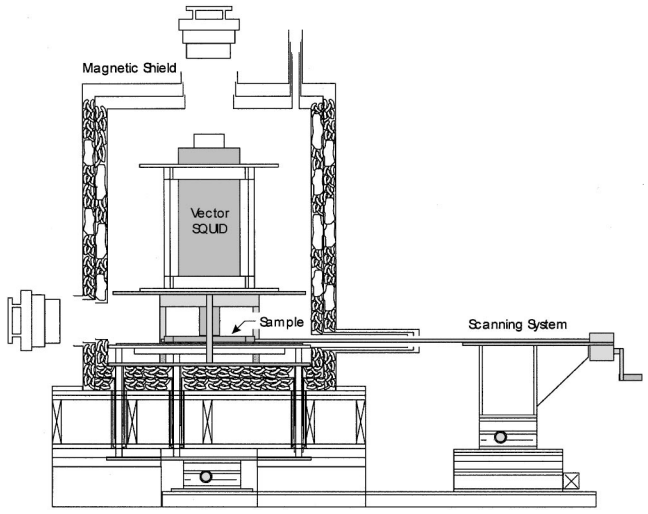

FIG. 6. The SQUID is supported in the center of the shield by a framework of G-10 and aluminum. The kinematic design of the frame simplifies the adjustment of rotation and tilt of the pickup coils with respect to the scanning coordinate system. The shield is mechanically isolated from the scanning system to prevent contact-induced vibrations.

of the magnetometer (i.e., less than 10^{-7} T), hence the dc shielding factor measured after de-Gaussing was more than 66 dB.

The SQUID is supported in the center of the shield by a framework of G-10 and aluminum that provides for kinematic positioning of the Dewar, as well as adjustment of rotation and tilt to simplify alignment of the SQUID coils with the scanning coordinate system. Figure 6 illustrates how the SQUID magnetometer, magnetic shield, and the sample scanning system are integrated in the magnetic imaging system.

1. Vibration isolation

Mechanical vibrations of the shield produce time-varying magnetic fields, which can be sensed by the magnetometer and may severely affect the quality of data, especially when measuring weak magnetic fields such as those associated with corrosion currents. Hence, the shield was mechanically isolated from the sample-scanning system to prevent contact-induced vibrations. To reduce the coupling to ground vibrations, the shield base was supported at six sites with damping pads. At each site, a vertical stack of six, $15\times7\times0.6$ cm vibration isolation pads (Isolation Technologies, NY), separated by 1.2-mm-thick aluminum sheets, provided the desired damping factor. The scanning stage rests on four $6\times6\times0.6$ cm Vibex pads sandwiched between the floor and 6-mm-thick aluminum plates.

III. DATA ACQUISITION

All stepper motor and data acquisition parameters are controlled through software that we wrote using LabVIEW® (National Instruments™, Austin, TX) and Motion Toolbox® (Compumotor Division, Parker Hannifin Corp., Rohnert Park, CA). The system is capable of data acquisition in four different modes. The continuous and the stop-and-go raster scan modes produce surface images. The stationary time-

base mode allows for temporal data acquisition from a specific location above the sample, and the raster time-base mode allows for repetitive data acquisition along a specific scan line. The effects of high-frequency noise are reduced through oversampling and averaging by the data acquisition software. Low- and high-pass filtering, gain, dc baseline, and other SQUID parameters are set through the SQUID controller.

A. Data acquisition modes

1. Stop-and-go raster scan mode

In the stop-and-go raster scan mode, the user selects the maximum and minimum travel limits, and the step size for each scan axis; the software selects the specified grid points within this area. The scanning system positions the sample under the magnetometer at the specified grid points, waits for an operator-specified time prior to data acquisition for any vibrational transients to die down, and acquires the specified number of samples at the desired rate. The average of these samples is then recorded. This approach has the advantage of ease in programming, but the greater disadvantages of slow speed, agitation of corrosive solutions due to numerous acceleration/deceleration periods, and increased cumulative positioning error, and hence is seldom used.

2. Continuous raster scan mode

In the continuous raster scan mode, data are acquired as the sample is scanned under the magnetometer at a constant speed along the fast axis of the scanning system. To minimize backlash and vibrations, and to allow room for acceleration of the stage to the desired speed, the scan line starts 5 mm outside the scan area. The acceleration of the motor is controlled by the software to ensure that the sample will reach the desired scanning speed within the first 2.5 mm of travel. To provide a consistent starting point for data acquisition, the motor indexer confirms that for each scan line the desired constant speed has been achieved, and then triggers the data acquisition as the initial sampling location is reached. To ensure accurate spatiotemporal sampling, data acquisition is carried under hardware control, using the AT-MIO onboard timing circuitry, rather than the main CPU clock of the computer. To minimize any hysteresis in the positioning of the sample due to friction between the glass surface of the scanning table and the Teflon feet of the carriage, and to minimize the associated vibrations, data are acquired only as the sample is pulled under the magnetometer rather than pushed. After each scan line, the sample is then moved one step along the perpendicular y axis and pushed back to the starting x coordinate. The process is repeated until the desired scan area has been covered.

3. Stationary time-base mode

In this mode, the desired location of the sample is positioned under the magnetometer and data acquisition is conducted for the user-defined duration, sampling rate (up to 6 kHz for each SQUID channel), and decimation factor.

TABLE I. Variables used for the analysis of spatial and temporal sampling.

Variable	Name	Units
v	Speed of stage	(mm/s)
N_d	Decimation factor	(dimensionless)
N_0	Oversampling factor	(dimensionless)
Temporal		
f_{mc}	Magnetometer low-pass cutoff frequency	(s^{-1})
f_N	Nyquist temporal sampling frequency	(points/s)
f_a	Actual temporal sampling frequency	(points/s)
Spatial		
k_{ic}	Image low-pass cutoff spatial frequency	(mm^{-1})
k_N	Nyquist spatial sampling frequency	(points/mm)
k_d	Desired spatial sampling frequency	(points/mm)
k_a	Actual spatial sampling frequency	(points/mm)
k_{oc}	Object cutoff spatial frequency	(mm^{-1})
k_{mc}	Magnetometer cutoff spatial frequency	(mm^{-1})

4. Raster time-base mode

The raster time-base mode is similar to the continuous raster scan mode with the exception that the sample is repeatably scanned along the x axis at a fixed y coordinate. At the end of each scan line, data acquisition is delayed for a user-specified period of time before repeating the same scan. This mode is especially useful for tracking rapid changes in the field over a particular region of the sample.

B. Spatial and temporal sampling

In imaging that utilizes spatial scanning of SQUID magnetometers, there are a number of variables that affect image resolution. There are tradeoffs between spatial and temporal resolution, and scanning speed. To obtain the best image, it is important to understand the relationship and limitations of these variables. We will analyze these in only one dimension; the results are directly applicable to two-dimensional images. The relevant variables are listed in Table I.

1. Spatial domain

We will consider the object that we are imaging to be a source of magnetic field, for example a distribution of current or magnetization. The image we obtain is a map of the magnetic field measured by the magnetometer. The object, $O(x)$, has a spatial frequency spectrum, $0(k)$, for spatial frequencies lower than the object cutoff frequency k_{oc}. We assume that there is no information for $k>k_{\mathrm{oc}}$, i.e.,

$$0(k)\approx 0, \quad \text{for } k>k_{\mathrm{oc}}. \tag{1}$$

If the cutoff is not sharp, a 3 dB point can specify k_{oc} and the other cutoff frequencies used in this analysis.

For our measurements, the SQUID magnetometer is some distance from the object. Because of the finite size of the sensor and the attenuation of magnetic field with distance from the object, the magnetometer acts as a spatial low-pass filter.[15–18] Thus we can only obtain information for spatial frequencies lower than the magnetometer cutoff frequency, k_{mc}. The spatial response of the magnetometer is given by $h(k)$, where we assume that

$$h(k)\approx 0, \quad \text{for } k>k_{\mathrm{mc}}. \tag{2}$$

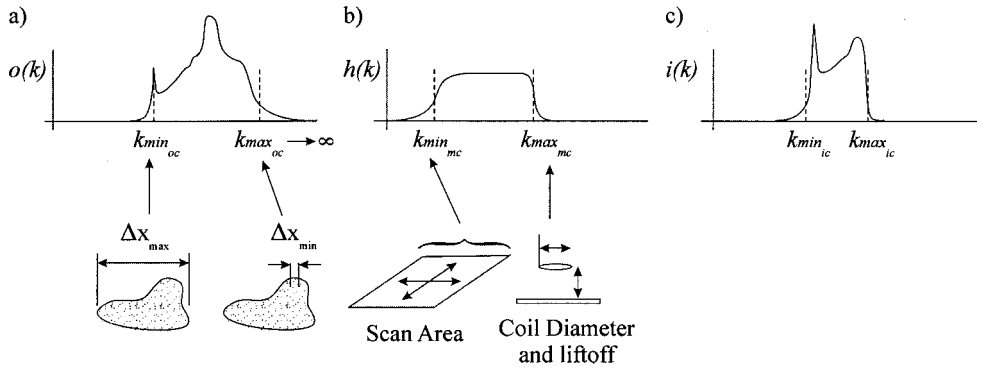

FIG. 7. Imaging in the spatial frequency domain; (a) the frequency spectrum of an object. The minimum object spatial frequency $k_{\min_{oc}}$ is limited by the physical dimensions of the object, $\Delta x_{\max}$. The size and distribution of the smallest features within the object, $\Delta x_{\min}$, determines the shape and value of the maximum object cutoff frequency $k_{\max_{oc}}$; (b) the frequency response of magnetometer. The minimum magnetometer spatial cutoff frequency $k_{\min_{mc}}$ is determined by the dimensions of the scan area. The maximum magnetometer spatial cutoff frequency $k_{\max_{mc}}$ is set primarily by the larger of the pickup coil diameter or liftoff (i.e., the magnetometer spatial resolution). (c) The resulting image frequency spectrum $i(k)$ is the product of the object and magnetometer spectra.

Quite often, the magnetometer spatial cutoff frequency is lower than the object cutoff frequency, or

$$k_{\mathrm{mc}} < k_{\mathrm{oc}}. \tag{3}$$

The image, $I(x)$, is the sampled magnetic field obtained by the scanned magnetometer. In the spatial frequency domain, the image $i(k)$ is given by

$$i(k) = h(k)0(k). \tag{4}$$

The spatial cutoff frequency of the image, k_{ic}, determined by both k_{oc} and k_{mc}, as shown in Fig. 7, provides a convenient measure of the highest spatial resolution achievable with that magnetometer. The spatial sampling used to record the image must obey the Nyquist theorem, in that

$$k_N \geqslant 2k_{\mathrm{ic}} \approx 2k_{\mathrm{mc}}. \tag{5}$$

2. Temporal domain

In cases where the magnetometer is scanned at a constant velocity relative to the object, the spatial frequencies are manifest at the time of recording as temporal frequencies. The challenge is to understand how to relate the temporal and spatial frequencies and to avoid aliasing of either image or noise at the time of recording.

For simple magnetometers, it is reasonable to assume that the temporal cutoff frequency, f_c, is the highest temporal frequency of information that could be present while recording the image, as determined by the antialiasing filter on the data acquisition system or the magnetometer. According to the Nyquist theorem, to prevent data aliasing, at least two samples must be made per cycle at the cutoff frequency. The Nyquist temporal frequency, f_N, is the minimum sampling frequency set by the Nyquist limit, i.e.,

$$f_N = 2f_{\mathrm{mc}}. \tag{6}$$

In practice the actual temporal sampling frequency, f_a, is larger than f_N by the oversampling factor N_0, or

$$f_a = N_0 f_N. \tag{7}$$

3. Space and time

For a scan at velocity v, the Nyquist spatial frequency, k_N, is the Nyquist temporal frequency divided by scanning velocity

$$k_N = 2\pi f_N / v. \tag{8}$$

The actual spatial sampling frequency, k_a, is the actual temporal sampling frequency divided by the stage speed

$$k_a = 2\pi f_a / v. \tag{9}$$

If k_a is greater than the desired spatial frequency, k_d, the extra samples can be eliminated by decimating the signal. One way to do this is to average groups of points, thereby reducing the number of samples in the image. The number of points to be averaged is simply

$$k_a / k_d = N_d, \tag{10}$$

which defines the decimation factor. If the temporal noise in the signal is incoherent, the signal-to-noise ratio will be improved by a factor of $\sqrt{N_d}$. Note that if the scanning velocity is set too high for a chosen sampling frequency, f_a, and cutoff frequency, f_{mc}, it is possible for the resulting spatial sampling frequency to violate the Nyquist limit in space. It is important to confirm that

$$k_a > 2k_{\mathrm{mc}}. \tag{11}$$

Table II shows an example of the settings used for the above variables in a typical scan.

In imaging of samples where the magnetic field changes in time, the goal is to optimize not only the spatial resolution, but also the temporal resolution of the scanned image. The effective temporal resolution provided by sequential images depends on the time it takes to scan the entire image; and hence, increasing the speed of the scan improves its temporal resolution. However, for a given spatial resolution, the increase in speed of the stage results in an increase in the required sampling frequency. Since the data acquisition card has a maximum analog-to-digital conversion rate, there is an upper limit to the scanning frequency, and hence the scanning speed. At this regime, a further increase in speed may

TABLE II. Example of the settings used for a typical SQUID scan.

1 Magnetometer low-pass filter set at 500 Hz	$f_{mc}=500\ s^{-1}$
2 Nyquist temporal sampling frequency is 1 kHz [Eq. (6)]	$f_N=1000$ points/s
3 Oversample by a factor of 2	$N_0=2$
4 Actual temporal sampling frequency set to 2 kHz [Eq. (9)]	$f_a=2000$ points/s
5 Stage speed is set at 30 mm/s	$v=30$ mm/s
6 Nyquist spatial sampling frequency is 33.3 points/mm [Eq. (6)]	$k_N=33.3$ points/mm
7 Actual spatial frequency is 66.7 points/mm	$k_a=66.7$ points/mm
8 For a pickup coil with a radius of 1 mm positioned less than 1 mm from the sample, the cutoff frequency is 3.8 mm^{-1}[a]	$k_{mc}=3.8\ mm^{-1}$
9 Confirm that the actual spatial frequency is at least twice the coil cutoff spatial frequency [Eq. (11)]	$k_a>7.7$ points/mm
10 From knowledge of the sample and the SQUID, the desired spatial frequency is set at 2 points/mm	$k_d=2$ points/mm
11 The decimation factor is 33	$N_d=33$

[a]Reference 19.

result in spatial undersampling and loss of spatial resolution. Furthermore, increasing f_a requires either a reduction of the oversampling and decimation factors or a wider magnetometer bandwidth, which reduces the signal-to-noise ratio. Consequently there are tradeoffs between spatial and temporal resolution and signal-to-noise ratio, and for each system one should optimize the above factors to achieve the desired spatiotemporal resolution and sensitivity.

C. System stability and long-term studies

1. Factors affecting signal stability

Corrosion of aluminum can be a slow process: in typical 40 year service lifetime, a military aircraft may lose through corrosion 10% of the thickness of a 1.2 mm thick fuselage skin, and that only in selected areas. The electrochemical dissolution of 100 μm of aluminum over 40 years produces a total current of approximately 150 nA/cm^2. The magnetic field from such corrosion activity could be as large as 7 pT at the surface of the metal, but may be orders of magnitude smaller due to corrosion currents flowing over very small spatial scales that do not contribute significantly to the magnetic field outside the sample.[4] While scanning SQUID magnetometers are capable of imaging these weak fields, the weakness of the magnetic field from slow corrosion and the fact that the field strength varies only slowly with time presents particular challenges, particularly because of the increase of both SQUID and environmental noise with decreasing frequency.

Because the experimenter cannot readily modulate the level of activity of the corrosion process, common lock-in amplifier techniques cannot be used to upconvert the very low frequency corrosion activity into a narrow bandwidth at higher frequencies, where the effects of SQUID and environmental noise are less significant. Because the sample can be scanned relative to the SQUID, the next obvious technique for eliminating the effects of these two noise sources is to have each scan extend sufficiently far beyond the sample that the magnetometer is no longer affected by the sample. At that distant reference point, ideally the sole contributions to the magnetometer output are the magnetic field within the shield and any offset, e.g., drift, that has appeared on the magnetometer output since the last time the magnetometer was at the reference point. (Because the nonmagnetic sample is scanned while the SQUID is held stationary, any gradients in the magnetic field within the shield do not affect the images.) The magnetometer output at the end of such a scan can then be subtracted from all data points elsewhere along the scan, thereby correcting for drift in the environmental magnetic field and the magnetometer output. This process is the spatial equivalent of the classical technique of using temporal chopping in a dc-coupled measurement. As we will see later in this section, the implementation of this approach with scanning SQUID magnetometers presents its own set of difficulties.

If the sample were perfectly nonmagnetic and isothermal, the corrosion activity would be the only source of magnetic field, and the measurement of the time dependence of corrosion over the course of days or weeks would be straightforward: the instantaneous magnetic field would be determined solely by the instantaneous corrosion activity. However, even nonferrous materials such as aluminum aircraft components can exhibit remnant magnetization from ferromagnetic contamination or inclusions that are orders of magnitude larger than the magnetic field due to corrosion. As long as the remanent magnetic field is stable in time, and any ongoing corrosion activity can be temporarily halted (for example, starting with a dry sample or by dehydrating an old, wet one through vacuum baking), the fields due to remanent magnetization can be measured independently to provide a reference image that can be subtracted from subsequent images that are recorded when corrosion is occurring. Subtraction of images recorded days or weeks apart places new constraints on system stability. If the remanent magnetization is not stable in time, for example, because of thermal relaxation or corrosion of the magnetized material, it may be difficult to delineate these field sources from corrosion. The obvious solutions are to avoid ferromagnetic contamination of the samples and to use ac demagnetization in a low ambient magnetic field to minimize the remanent magnetization.

Given the weakness of the corrosion magnetic field, the SQUID must be operated either in a high sensitivity mode, i.e., with a high gain within the flux-locked loop, or with a high gain after the flux-locked loop. The presence of dc offsets from instrument drift, the environmental field, or remanent magnetization in the sample can limit the total gain that

can be used. If the magnetometer and the data acquisition system are both dc coupled, then any substantial drifts and offsets will require a large dynamic range in both the flux-locked loop and the analog-to-digital converter (ADC). Since the corrosion signals can be small relative to the drifts and offsets, a 16-bit or higher resolution ADC may be required to avoid the addition of quantization noise to the corrosion signal.

2. Removal of drift and offset

a. Electronic offset subtraction. At the beginning or end of each scan, it is possible to remove offsets on the SQUID output prior to a high gain amplifier and the ADC by using a sample-and-hold circuit at the inverting input of a differential amplifier. We constructed an offset reset controller (ORC) which contained a sample-and-hold circuit with a sufficiently low drift capacitor to hold a reference voltage without significant drift for the length of time required to complete a typical scan line. The scanning software was modified to position the sample under the magnetometer at a particular reference point on each scan line, away from the corrosion site, and to trigger the ORC to store the reference voltage prior to the start of data acquisition for each scan line. The sample was then scanned under the magnetometer in the usual stop-and-go fashion and the SQUID output was subtracted electronically from the reference voltage stored in the ORC. This procedure was repeated until the desired area had been scanned. This technique can reduce the offset in a software-controlled manner, restricted by changes in offsets during a single scan. For our measurements, we found that a drifting offset limited the use of the ORC to relatively small scan areas and short-term studies. Because the ORC had to be placed before the high-gain amplifier, it contributed noise to the low-level signals from weak corrosion.

b. Offset removal by filtering. A lower noise and technically simpler solution for removing drifts and offsets prior to high-resolution digitization was to ac couple the SQUID output to the ADC by means of high-pass filter in the SQUID controller (3 dB at 0.3 Hz). While corrosion is a quasi-dc process, our scanning approach and our restricted sample size allow us to filter out the very lowest frequencies.

In the continuous raster scan mode, the spatial frequencies in the magnetic field distribution are manifest as temporal frequencies scaled by the speed of the scan. A temporal high-pass filter applied to the SQUID output attenuates all temporal frequencies below the high-pass cutoff frequency ($f_{\mathrm{hc}}=0.3\,\mathrm{Hz}$). To convert this value to spatial frequency, in units of mm^{-1}, we divided by the scanning speed v measured in mm/s

$$k_{\mathrm{hc}}=2\pi f_{\mathrm{hc}}/v. \tag{12}$$

The scanning speeds used by the system range from 10 to 60 mm/s. As a worst case scenario, for the minimum scanning speed of 10 mm/s, the application of the 0.3 Hz temporal high-pass filter only attenuates spatial frequencies lower than 0.02 mm^{-1}. This spatial frequency suggests that, for this speed, the high-pass filter will attenuate spatial data corresponding to source separations of order of 33 mm and above. In practice, the source separations for our samples are much smaller than the limit set by the high-pass filter, in fact, for all scanning speeds within the above-mentioned range, ac-coupled data acquisition results in no significant loss of data and allows the system to operate with a larger analog gain than would otherwise be possible. The major disadvantage of this approach is that it does not remove drift at the input of the SQUID so that occasionally the SQUID will exceed the dynamic range of the flux-locked loop and will automatically reset. The resulting jump in the output will be high-pass filtered and will produce a long tail with an exponential time constant equal to that of the high-pass filter. This transient can then be removed by signal processing with only minor loss of data. A possible alternative would be to couple this process with a digital reset of the SQUID at the beginning of each scan.

While filtering is an affective solution to the drift and gain problems, the Ac-coupled magnetic field waveforms $B'(t)$ differ from the true, dc-coupled magnetic field $B(t)$ by a term proportional to the integral of the observed signal divided by the effective time constant τ of the system[20,21]

$$B(t)=B'(t)+1/\tau\int B'(t')dt'. \tag{13}$$

The time constant τ of the system was experimentally measured to be 0.53 ± 0.04 s. Equation (13) can, for our measurements, be converted to a discrete summation over the spatial-sampling positions x_i:

$$B(x_i)=B'(x_i)+\frac{\Delta x}{v\tau}\sum_{x_i} B'(x_i), \tag{14}$$

where $x_i=i\Delta x$, for $i=1,2,...,i_{\max}$, and $i_{\max}$ corresponds to the total number of sampling sites along the x axis and we have replaced dt with $\Delta x/v$.

This expression reveals the velocity dependence of the observed signals. We can use Eq. (14) to recover the original signal up to an additive constant that is equivalent to an arbitrary dc offset. Figure 8 demonstrates how the above transformation recovers the original signal $B(x)$ from the observed signal $B'(t)$, measured at five different scanning speeds, above a 2-cm-diameter loop of wire carrying 0.25 mA of current.

Since the conversion of the observed signal to the actual magnetic field includes a line-by-line spatial integration of each raster scan, the scan area should be selected large enough to contain essentially all of the magnetic field of the corroding region. Since the dc baseline for each scan line is determined by the value of the first data point in that line, variations in this value between lines will change the dc level for that line; if the variation is large enough, there will be a line-by-line dc shift, which could either be a true contribution from the sample or due to system drift. Although most of these shifts can be removed from the image by postprocessing, the appropriate preventative technique, carried on at the time of the scan, is to enlarge the scan area to include ample margins around the corroding area where the magnetic field does not contain large lateral (line-to-line) gradients. This reduces the possibility of artifacts and minimizes the time required for postprocessing computations. A refinement of this approach is to make one or more scans along the line

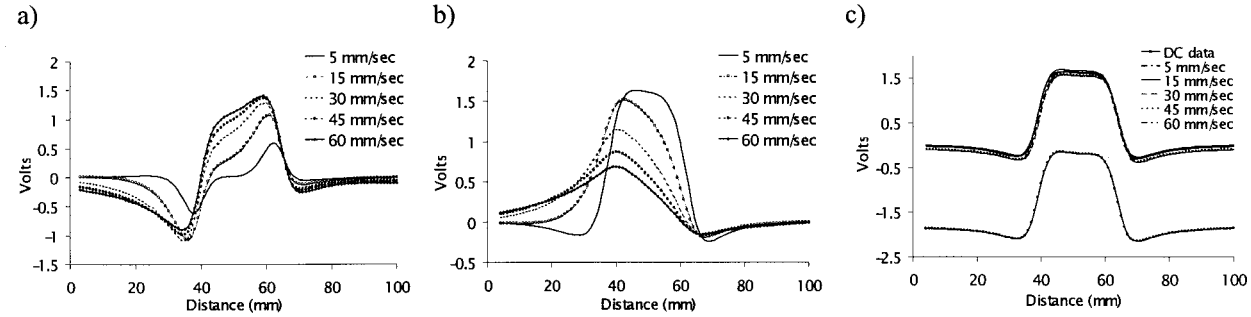

FIG. 8. Converting the ac-coupled magnetic field waveforms $B'(x)$ to the true, dc-coupled, waveforms $B(x)$. (a) The output of the magnetometer in the ac mode, $B'(x)$, for five different scanning speeds. The source of magnetic field is a 2-cm-diameter coil carrying a dc current of 0.5 mA. (b) The correction term for each speed (i.e., the term containing the summation in Eq. (14). (c) The comparison of the recovered magnetic field [$B(x)$ in Eq. (14)], with the actual output of magnetometer in the dc mode (lower curve). In the above data, the actual magnetic field is recovered, with the exception of the dc baseline, to better than 3%.

of reference positions or even around the entire perimeter of the scanned area to determine the field distribution around the edges, and to use these values, rather than an assumed zero field at the reference points, as the constraint in the restoration.

IV. NOISE SOURCES AND REDUCTION

Typically, magnetic fields due to corrosion are no larger than a nano-Tesla, so that the system noise can be an extremely important limiting factor in measurements of weakly corroding samples. We previously discussed how the proper selection of sampling rate and both analog and digital filtering are required to optimize the signal-to-noise ratio of the images. Even more important is to address system noise from ground loops and electromagnetic interference from dc to rf. The major sources of noise for our system are described below.

A. Ground loops

Careful attention was paid to ground loops which would otherwise result from the interconnection of a large number of different electronic instruments. To remove this problem, the building earth ground was connected to the SQUID electronics and the Faraday cage that enclosed them, and hence to the data acquisition card via the cable shield. The card thereby provides the ground to the computer chassis. Since both the motor electronics (via the motor controller card), and the computer monitor (via the VGA cable), were connected to the computer, the computer and monitor were powered through an isolation transformer (Stancor, GIS-500), and the motor control electronics (AT6400, and zeta drives) were powered through another isolation transformer (Stancor, GIS-1000).

B. Stepper motor electronics noise

Stepper motors and their drive amplifiers generated substantial electromagnetic noise which required significant attention to shielding and elimination of ground loops; newer designs of motors and amplifiers, or dc motors, may reduce this problem. We addressed this problem by placing the motor-control electronics in a metal chassis, by routing the motor cables through braided shields, and by locating the stage and its motors away from the magnetometer. Also, we reduced the remaining high frequency contribution from motor drive electronics by low-pass filtering of the magnetometer output prior to data acquisition.

C. rf shield

Since our SQUID system did not include an integral cryogenic rf shield, it proved to be sensitive to rf radiation. To minimize this problem, SQUID flux-locked loop electronics, and the control electronics were placed in a pair of aluminum rf shields connected by rigid copper pipe. Power for the SQUID controller was provided by rf feedthroughs. The entire rf shielding assembly was grounded via a low-resistance conductive path to the main ground. The electrical cables between the FLL and the iMAG were threaded through toroidal filter cores (Part No. 5977003801, Fairwrite Products Corp., Wallkill, NY).

D. SQUID jumps

Possibly because of the lack of a rf shield, or as a result of the design of the Conductus SQUID sensors, the SQUIDs occasionally exhibited excess noise or flux jumps in all channels, mostly triggered either by the *y*-axis channel itself, or by noise preferentially detected by that channel. For many studies, we utilize only the *z*-axis channel and achieve greater system stability.

V. ADDITIONAL ISSUES

A. Heaters

Due to high humidity in the lab, and the 5 liter per day boil off of the Dewar with the closely spaced tail, we encountered condensation on the connectors between the SQUID sensors and the flux-locked loop. This problem was solved by installing 30 Ω, coaxial resistance heaters on each connector, connected to a 10 V dc-power supply (Hewlett Packard, E610A).

B. System calibration, tilt/rotation adjustment, and centering

We devised a sample holder equipped with coils and wires for calibration, rotation, tilt adjustment, and centering

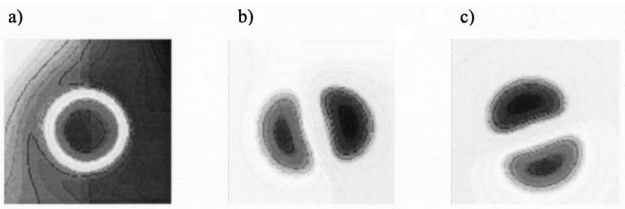

FIG. 9. A simple technique for determination of the position, orientation, and tilt of the SQUID pickup coils with respect to the scanning coordinates. Images (a), (b), and (c) represent the simultaneously measured *z*, *y*, and *x* components of the magnetic field above a 2-mm-diameter loop of wire carrying a current of 0.5 mA. The axis of symmetry in (b) and (c) suggest that a clockwise rotation of the SQUID Dewar by 21 degrees is necessary for alignment of the *x*- and *y*-component coil axes. The difference in the magnitude of the positive and negative peaks in both *x*- and *y*-coordinate images provides the necessary information for adjustment of the dewar tilt to align the axis of the *z*-pickup coil to be perpendicular the surface of the scanning table.

of the SQUID magnetometer with respect to the scanning coordinates. We used two wires forming a cross hair, centered about the sample holder, to determine the relative position of the pickup coils with respect to scanning coordinates. A 2-cm-diameter loop, also centered about the sample holder, allowed us to determine the orientation of the *x* and *y*-pickup coils with respect to scanning coordinates and to level the pickup coils with respect to the scanning table. We used two 30 cm long, straight wire segments for calibration of the magnetometer by comparing the measured image of the magnetic field due to a known current flowing through each wire with its predicted value.

VI. PRELIMINARY DATA

A. Alignment of the pickup-coil axes with the scanning system

Figure 9 shows the simultaneously measured components of the magnetic field above a 2-cm-diameter loop of wire carrying a current of 0.5 mA. The image was obtained for the subsequent alignment of the coil axes with the scanning coordinates. The orientation of the symmetry axis of the images of *x* and *y* components of magnetic field determines the rotation angle necessary to align the coil axes with the scanning coordinates. The difference in magnitude of the positive and negative peaks in both *x*- and *y*-coordinate images provides the information necessary for us to tilt the dewar to align the axis of the *z*-pickup coil perpendicular to the surface of the scanning table.

B. Aluminum corrosion

The bottom surface of a 7 cm diameter, 1.2 mm thick disk of 7075-T6 aluminum was exposed to a 0.5 M NaOH solution at room temperature for a period of 33 h. The images shown in Fig. 10 present the change in the *z* component of the magnetic field above the corroding sample for the first 18 h of this experiment. All data are subtracted from the first (dry sample) image. Clearly, the change in magnetic field is localized to the area of the sample and displays complex spatial and temporal structures at spatial scales of several millimeters or larger.

C. Detection of slow corrosion

The bottom (hidden) surface of a 2024-T3 aluminum plate, with dimensions of $75\times75\times1.2$ mm, was exposed at room temperature to a slow-corrosion cocktail typical of that found in old aircraft lap joints.[22] Figure 11 represents the photograph of the corroded surface of the plate and the cumulative magnetic activity of the sample recorded over 190 h of exposure. This experiment demonstrates that the system is sufficiently sensitive to detect corrosion activity at nonaccelerated, realistic, corrosion rates.

VII. DISCUSSION

The SQUID magnetometer system reported in this article was designed for noninvasive measurements of the rate

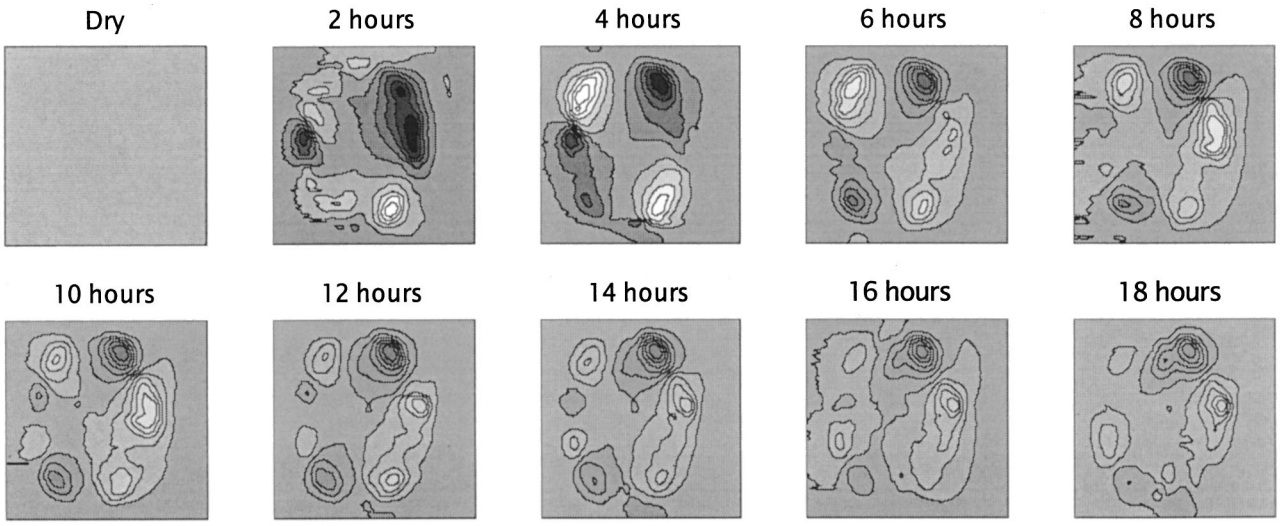

FIG. 10. Spatiotemporal variation in magnetic field of an aluminum sample undergoing hidden corrosion. The bottom surface of a 7 cm diameter, 1.2 mm thick, disk of 7075-T6 aluminum was exposed to a 0.5 M NaOH solution for 33 h. The above images present the change in the *z* component of the magnetic field due to electrochemical corrosion for the first 18 h of the experiment. The magnetic activity is localized to the area of the sample and exhibits complex spatial and temporal structure.

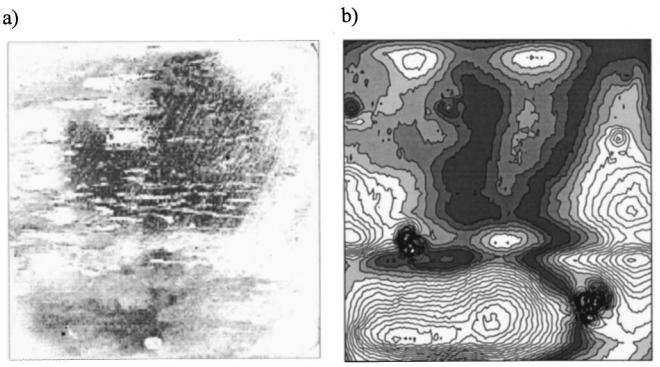

FIG. 11. Noninvasive detection of slow, hidden corrosion. (a) Photomicrograph of the lower (hidden) surface of a 3-in. square sample of 2024-T3 aluminum that was exposed to a corrosive solution typical of an aircraft lap joint. The dark gray area in the upper center of the image corresponds to noncorroded aluminum. (b) The cumulative magnetic activity of the sample showing the more active regions in white and the less active ones in dark gray.

of hidden corrosion in aircraft aluminum alloys with planar geometries; however, its use can be extended to all nonmagnetic metals. The kinematic design and automation capabilities incorporated in the system allows for long-term studies (months), as well as repeatable measurements of the corrosion magnetic field of multiple samples. This feature, coupled with the magnetic and rf shielding, makes the system ideal for laboratory investigation of hidden corrosion for various metal-solution combinations covering a large spectrum in corrosivity. Furthermore, the system has the sensitivity to detect (in real time) the magnetic field due to extremely low corrosion rates typical of aircraft lap joints; at these rates it often takes years before the corrosion-related thickness loss of the aircraft fuselage can be measured by other noninvasive techniques. This provides a unique advantage in using the SQUID magnetometers for hidden corrosion studies.

We are in the process of utilizing this instrument in a pair of studies of corrosion in aircraft aluminum. The first is designed to determine the quantitative relationship between corrosion activity and magnetic field, and utilizes samples with a carefully controlled geometry.[23,24] The second involves nondestructive measurements of corrosion in lap joints removed from aging KC-135 and Boeing-707 aircraft.[25] Other applications under consideration include the magnetic measurement of filiform corrosion under paint, exfoliation corrosion within thick aircraft wing planks, and the effectiveness of corrosion prevention compounds in preventing hidden corrosion.

Because properly prepared and treated aircraft do not corrode rapidly, the magnetic fields associated with corrosion in aircraft aluminum are weak relative to the geomagnetic field, environmental magnetic noise, the magnetic field from ferromagnetic fasteners, and the magnetic fields resulting, from thermoelectric currents associated with temperature gradients and galvanic fields associated with contact between dissimilar metals. Each of these other field sources can be controlled in a laboratory environment either through magnetic shielding, the use of the stationary magnetometer or gradiometer, or proper sample preparation and degaussing techniques. There will be, of course, certain types of samples, such as ones with large ferromagnetic fasteners, for which it may be difficult to separate the corrosion signal from that due to other sources. However, at present it seems unlikely that this technique can be extended to measurements of corrosion signals in intact aircraft on the flight corrosion line. Even so, there is ample research that can be conducted with a laboratory SQUID instrument that is not possible with any other measurement technique.

The SQUID magnetometer system we describe should prove to be a valuable laboratory tool for understanding the principles underlying the generation of the corrosion magnetic field and for developing appropriate models that relates the spatiotemporal variations in corrosion magnetic field to corrosion rate, spatial distribution, and perhaps the type of hidden corrosion. The preliminary data clearly show complex spatiotemporal variations in corrosion magnetic field, which suggest that a subset of corrosion information can be measured noninvasively with this instrument. This information may be invaluable for better understanding the dynamics of hidden corrosion, and for developing realistic models that can predict the long-term behavior and rate of corrosion in occluded regions.

ACKNOWLEDGMENTS

The authors would like to thank Anthony P. Ewing for his editorial suggestions and Carlos Hall for his valuable comments regarding spatial aliasing. This work was supported in part by NCI Information Systems, Inc. through Air Force Contract No. F09603-97-D-0550, Task Order 9128-002, and by AFOSR Grant No. F49620-93-0268.

[1] J. R. Kirtley and J. P. Wikswo, Jr., Annu. Rev. Mater. Sci. **29**, 117 (1999).
[2] J. G. Bellingham, M. L. A. MacVicar, M. Nisenoff, and P. C. Searson, J. Electrochem. Soc. **133**, 1753 (1986).
[3] J. G. Bellingham, M. L. A. MacVicar, and M. Nisenoff, IEEE Trans. Magn. **23**, 477 (1987).
[4] A. D. Hibbs, J. Electrochem. Soc. **139**, 2447 (1992).
[5] B. D. Jette and M. L. A. MacVicar, IEEE Trans. Magn. **27**, 3025 (1991).
[6] M. Misra, S. Lordi, and M. L. A. MacVicar, IEEE Trans. Magn. **27**, 3245 (1991).
[7] A. D. Hibbs, R. E. Saeger, D. W. Cox, T. H. Aukerman, T. A. Sage, and R. S. Landis, Rev. Sci. Instrum. **63**, 3652 (1992).
[8] D. S. Buchanan, D. B. Crum, D. Cox, and J. P. Wikswo, Jr., *Advances in Biomagnetism*, edited by S. J. Williamson, G. Hoke, G. Stroink, and M. Kotani (Plenum, New York, 1990), p. 667.
[9] Y. P. Ma and J. P. Wikswo, Jr., Rev. Sci. Instrum. **62**, 2654 (1991).
[10] D. Li, Y. P. Ma, W. F. Flanagan, B. D. Lichter, and J. P. Wikswo, Jr., *Proceedings of the Tri-Service Conference on Corrosion Washington, DC*, (Department of Defense, 1994), p. 335.
[11] D. Li, Y. P. Ma, W. F. Flanagan, B. D. Lichter, and J. P. Wikswo, Jr., J. Min. Metals Mater. **47**, 36 (1995).
[12] D. Li, Y. P. Ma, W. F. Flanagan, B. D. Lichter, and J. P. Wikswo, Jr., Corrosion (Houston) **52**, 219 (1996).
[13] D. Li, Y. P. Ma, W. F. Flanagan, B. D. Lichter, and J. P. Wikswo, Jr., Corrosion (Houston) **53**, 93 (1997).
[14] W. G. Jenks, S. S. H. Sadeghi, and J. P. Wikswo, Jr., J. Appl. Phys. **30**, 293 (1996).
[15] B. J. Roth, N. G. Sepulveda, and J. P. Wikswo, Jr., J. Appl. Phys. **65**, 361 (1989).
[16] J. P. Wikswo, Jr., Electroencephalogr. Clin. Neurophysiol. **69**, 266 (1987).
[17] S. Tan, B. J. Roth, and J. P. Wikswo, Jr., Electroencephalogr. Clin. Neurophysiol. **76**, 73 (1989).
[18] *SQUID Sensors: Fundamentals, Fabrication and Applications*, edited by J. P. Wikswo, Jr. and H. Weinstock (1996).
[19] B. J. Roth and J. P. Wikswo, Jr., Rev. Sci. Instrum. **61**, 2441 (1990).

[20] J. P. Wikswo, Jr., J. P. Barach, and J. A. Freeman, Science **208**, 53 (1980).
[21] J. P. Barach, J. A. Freeman, and J. P. Wikswo, Jr., J. Appl. Phys. **51**, 4532 (1980).
[22] Provided by K. S. Lewis and R. G. Kelly at the University of Virginia. Listed as ion/ppm: Na/870; K/2335; Sr/48; Ca/53.2; Al/1914; Cu/28; Mg/1333; Mn/159; Zn/10; Cl/10; NO2/160; SO4/483; NO3/44; F/9; HPO4/841; HCO3/1611; acetate/2; Cl- acetate/0.03/propionate/9; butyrate/16; formate/1.
[23] A. Abedi and J. P. Wikswo, Jr. (unpublished).
[24] A. Abedi and J. P. Wikswo, Jr. (unpublished).
[25] R. G. Skennerton, A. Abedi, and J. P. Wikswo, Jr., J. Corr. Sci. Eng. (submitted for publication).